AGU PUBLICATIONS

JGR

Journal of Geophysical Research: Space Physics

RESEARCH ARTICLE
10.1002/2017JA024186

This article is a companion to Toth et al. (2017), https://doi.org/10.1002/2017JA024189.

Key Points:
- We performed a 1 h long global simulation of Earth's magnetosphere with kinetic modeling of the dayside reconnection
- Crater FTE is found at the early stage of a flux rope formation
- Kinetic phenomena are found from the global simulation

Correspondence to:
Y. Chen,
yuxichen@umich.edu

Citation:
Chen, Y., Tóth, G., Cassak, P., Jia, X., Gombosi, T. I., Slavin, J. A., … Henderson, M. G. (2017). Global three-dimensional simulation of Earth's dayside reconnection using a two-way coupled magnetohydrodynamics with embedded particle-in-cell model: Initial results. *Journal of Geophysical Research: Space Physics*, *122*, 10,318–10,335. https://doi.org/10.1002/2017JA024186

Received 24 MAR 2017
Accepted 8 AUG 2017
Accepted article online 18 SEP 2017
Published online 21 OCT 2017

Global Three-Dimensional Simulation of Earth's Dayside Reconnection Using a Two-Way Coupled Magnetohydrodynamics With Embedded Particle-in-Cell Model: Initial Results

Yuxi Chen[1], Gábor Tóth[1], Paul Cassak[2], Xianzhe Jia[1], Tamas I. Gombosi[1], James A. Slavin[1], Stefano Markidis[3], Ivy Bo Peng[3], Vania K. Jordanova[4], and Michael G. Henderson[4]

[1]Center for Space Environment Modeling, University of Michigan, Ann Arbor, MI, USA, [2]Department of Physics and Astronomy, West Virginia University, Morgantown, WV, USA, [3]Department for Computational Science and Technology, KTH Royal Institute of Technology, Stockholm, Sweden, [4]Los Alamos National Laboratory, Los Alamos, NM, USA

Abstract We perform a three-dimensional (3-D) global simulation of Earth's magnetosphere with kinetic reconnection physics to study the flux transfer events (FTEs) and dayside magnetic reconnection with the recently developed magnetohydrodynamics with embedded particle-in-cell model. During the 1 h long simulation, the FTEs are generated quasi-periodically near the subsolar point and move toward the poles. We find that the magnetic field signature of FTEs at their early formation stage is similar to a "crater FTE," which is characterized by a magnetic field strength dip at the FTE center. After the FTE core field grows to a significant value, it becomes an FTE with typical flux rope structure. When an FTE moves across the cusp, reconnection between the FTE field lines and the cusp field lines can dissipate the FTE. The kinetic features are also captured by our model. A crescent electron phase space distribution is found near the reconnection site. A similar distribution is found for ions at the location where the Larmor electric field appears. The lower hybrid drift instability (LHDI) along the current sheet direction also arises at the interface of magnetosheath and magnetosphere plasma. The LHDI electric field is about 8 mV/m, and its dominant wavelength relative to the electron gyroradius agrees reasonably with Magnetospheric Multiscale (MMS) observations.

1. Introduction

Magnetic reconnection between the interplanetary magnetic field (IMF) and Earth's intrinsic dipole field is regarded as the most important mechanism for mass and energy transfer from the solar wind to the magnetosphere. Flux transfer events (FTEs) are widely considered as a phenomenon related to dayside nonsteady reconnection (Russell & Elphic, 1978). An FTE is a bundle of reconnected magnetic flux tubes created at the magnetopause and moving antisunward along the magnetopause. Such events are characterized by a bipolar variation of the magnetopause normal magnetic field B_N and are usually associated with an enhancement of core field, the magnetic field component along the axial direction of the FTE. An FTE exhibits a flux rope structure in three-dimensional space. It has been observed that the plasma inside an FTE is usually a mixture of magnetospheric and magnetosheath plasma (Daly et al., 1981), indicating that FTEs are generated by magnetic reconnection process. The diameter of an FTE can vary from several ion inertial lengths (Eastwood et al., 2016) (a few hundred kilometers) to several Earth radii (Rijnbeek et al., 1984; Hasegawa et al., 2006). In the dawn-dusk direction along the magnetopause, FTEs can extend over a long distance (Fear et al., 2008). FTEs frequently occur as a quasi-periodic process, and Rijnbeek et al. (1984) reported that the FTEs were observed about every 8 min during periods of southward magnetosheath magnetic field.

FTEs have been studied with various global numerical models. Compared to local simulations, a global model can offer more realistic plasma and magnetic field context. Fedder et al. (2002) used a global ideal MHD model to study the generation of FTEs. The typical magnetic field signature is captured by their model, and their simulation suggests that the FTEs are formed by nonsteady reconnection along the separator at the magnetopause. Raeder (2006) performed a high-resolution ideal MHD simulation with the OpenGGCM model.

FTEs are formed by multiple X line reconnection (Lee & Fu, 1985) with a tilted dipole field in this study. Dorelli and Bhattacharjee (2009) revisited the FTE generation mechanism with resistive MHD using the OpenGGCM model, and the authors argue that the FTEs are generated by flow vortices and the formation of new X lines is the consequence, rather than the cause of FTE formation. Sibeck et al. (2008) studied crater FTEs with the Block-Adaptive-Tree-Solarwind-Roe-Upwind-Scheme (BATS-R-US) MHD model. All these global simulations are based on ideal or resistive MHD codes, and the generation of FTEs relies either on ad hoc resistivity (Dorelli & Bhattacharjee, 2009) or numerical resistivity (Fedder et al., 2002; Raeder, 2006). Recently, a 2D-3V global magnetospheric hybrid-Vlasov simulation was performed to study magnetopause reconnection and FTEs by Hoilijoki et al. (2017).

Typical FTEs are associated with an enhancement of the field strength at the center of a flux rope. On the other hand, the so-called crater FTEs show more complicated structure: the center field is surrounded by two "trenches" and the field strength usually show a dip just at the center (LaBelle et al., 1987; Owen et al., 2008). Typical FTEs are more frequently observed than crater FTEs (Zhang et al., 2010). The generation mechanism of crater FTEs has been explored with both numerical simulations (Sibeck et al., 2008) and analytic models (Zhang et al., 2010). Zhang et al. (2010) proposed that crater FTEs are the initial stage of typical FTEs based on hundreds of events selected from the Time History of Events and Macroscale Interactions during Substorms (THEMIS) observations. The structure of the core field can be even more complicated, for example, Eriksson et al. (2016) found a tripolar core field flux rope at the magnetopause.

It is widely accepted that the formation of FTEs is related to the dayside magnetopause reconnection, which is a kinetic process for collisionless plasma. Therefore, it is important to include proper kinetic effects into the numerical model in order to produce FTEs in a physical way. The MHD with embedded PIC (MHD-EPIC) model developed by Daldorff et al. (2014) makes it feasible for the first time to use a kinetic model to study reconnection and FTEs with realistic magnetospheric configuration. Because of the small kinetic scales inside the magnetosheath, for example, the ion inertial length d_i is about 60 km $\sim 1/100\, R_E$, we have to artificially increase the kinetic scales in the present 3-D global simulation. As shown by our companion paper Tóth et al. (2017), this scaling has no significant effect on the large-scale structures, while the kinetic phenomena occur at linearly increased scale. Since the kinetic scale physics is included in our global model, the reconnection related kinetic phenomena, like the crescent shape electron phase space distribution, the Larmor electric field, and the lower hybrid drift instability (LHDI) are all captured by the model. The crescent distribution was first found by Hesse et al. (2014) from 2-D local simulation and then observed by the Magnetospheric Multiscale (MMS) mission recently (Burch et al., 2016). It is formed by the magnetosheath electrons reaching the stagnation point and accelerated by the Hall electric field (Bessho et al., 2016; Shay et al., 2016). Recently, the origin of the crescent distribution is discussed by Lapenta et al. (2017) with a high-resolution multiscale simulation. This special distribution has been proposed as an indicator of the magnetic reconnection location (Hesse et al., 2014). The Larmor electric field is potentially another signature that can help to identify the location of reconnection site (Malakit et al., 2013). It is on the magnetosphere side, normal to the current sheet, and pointing away from the X line. The lower hybrid drift instability (LHDI) develops along the current direction (Daughton, 2003; Roytershteyn et al., 2012), and it has been observed recently by MMS satellites (Graham et al., 2016). LHDI was considered as a potential source to create anomalous resistivity for reconnection (Huba et al., 1977), but previous research (Mozer et al., 2011) has suggested that the related resistivity may be not large enough. However, a recent 3-D simulation showed LHDI may still play an important role near the diffusion region because of the presence of turbulence (Price et al., 2016).

In the following sections we will describe the MHD-EPIC model, the simulation setup, and then discuss the simulation results.

2. Model Description

The MHD-EPIC model has been successfully applied to investigate the interaction between the Jovian wind and Ganymede's magnetosphere, where the ion inertial length is large compared to the size of its magnetosphere (Tóth et al., 2016). In this paper, the same model is applied to study Earth's magnetosphere, which is more challenging because of the small kinetic scale. The MHD-EPIC model two-way couples the BATS-R-US (Powell et al., 1999; Tóth et al., 2008) MHD code and the implicit particle-in-cell code iPIC3D (Markidis et al., 2010) through the Space Weather Modeling Framework (SWMF) (Tóth et al., 2005, 2012). A general description of the these models and the simulation setup are provided in this session.

2.1. Global MHD Model: BATS-R-US

In order to make the MHD model as complete as possible, the Hall term and the electron pressure gradient term are included in the generalized Ohm's law, and a separate electron pressure equation is solved. The generalized Ohm's law we use is

$$\mathbf{E} = -\mathbf{u} \times \mathbf{B} + \frac{\mathbf{J} \times \mathbf{B}}{q_e n_e} - \frac{\nabla p_e}{q_e n_e}, \tag{1}$$

where q_e, n_e and p_e are the charge per electron, electron number density and electron pressure, respectively. The electron pressure is obtained from:

$$\frac{\partial p_e}{\partial t} + \nabla \cdot (p_e \mathbf{u}_e) = (\gamma - 1)(-p_e \nabla \cdot \mathbf{u}_e), \tag{2}$$

where $\gamma = 5/3$ is the adiabatic index, and $\mathbf{u_e} = \mathbf{u} - \mathbf{J}/(q_e n_e)$ is the electron velocity.

From the numerical perspective, it is not trivial to incorporate the Hall term into the MHD equations. The Hall MHD equations support the whistler mode wave, which is dispersive, and the characteristic speed is inversely proportional to the wavelength. Since the shortest wavelength that can be resolved in a numerical system is twice the cell size, the fastest whistler wave speed is proportional to $1/\Delta x$. For an explicit time integration scheme, the time step is limited by the Courant-Friedrichs-Lewy (CFL) condition, which leads to a time step approximately proportional to $1/(\Delta x)^2$ for Hall MHD. In order to use a reasonably large time step, a semi-implicit time discretization is employed (Tóth et al., 2012). The semi-implicit scheme treats the stiff terms, which is the Hall term here, and other terms separately. Excluding the Hall term, the rest of the equations are updated with an explicit scheme, and the time step is only limited by the fast magnetosonic wave speed. The Hall term is handled by an implicit solver after the explicit update has been done.

The typical solar wind condition at 1 AU with purely southward IMF is used as the boundary condition to drive the magnetosphere: $\mathbf{B} = (0, 0, -5)$ nT, mass density $\rho = 5$ amu/cm^3, ion pressure $p_i = 3.45 \times 10^{-3}$ nPa, and solar wind velocity $\mathbf{u} = (-400, 0, 0)$ km/s. Electron pressure $p_e = 8p_i = 2.76 \times 10^{-2}$ nPa is used, so that after crossing the shock, where the ions are heated by converting bulk into thermal energy while the electron thermal energy changes adiabatically, the ion-electron pressure ratio is about $p_i/p_e \sim 2.5$. Wang et al. (2012) show that the temperature ratio T_i/T_e in the solar wind varies from 0.1 to 2, and the ratio is about 4 to 12 inside the magnetosheath. The T_i/T_e ratio, which is the same as p_i/p_e, used in the simulation is close to but slightly smaller than the typical observed ratio. We use $T_i/T_e = 1/8$, because our numerical experiments show that the electrons can be numerically heated in the PIC code if colder solar wind electrons are used for the upstream boundary condition. A magnetic dipole with 30,116 nT field strength at the Earth magnetic equatorial surface is used. Its magnetic axis is aligned with the z axis. The total magnetic field $\mathbf{B}$ is split into the intrinsic dipole field $\mathbf{B_0}$ and the deviation $\mathbf{B_1}$. A three-dimensional block-adaptive Cartesian grid is used to cover the whole magnetosphere: $-224\,R_E < x < 32\,R_E$, $-128\,R_E < y < 128\,R_E$, and $-128\,R_E < z < 128\,R_E$. Since we focus on the dayside dynamics in this paper, the mesh along the dayside magnetopause is refined to high resolution with $\Delta x = 1/16\,R_E$ (see Figure 1). Fifty-nine million cells are used in total. At the inner boundary $r = 2.5\,R_E$, the density is fixed as 28 amu/cm^3, the pressure and the magnetic field $\mathbf{B_1}$ have zero gradient, the radial velocity is zero, while the tangential velocity is calculated from the ionosphere electrodynamics model developed by Ridley et al. (2004).

2.2. Implicit Particle-in-Cell Model: iPIC3D

The semi-implicit particle-in-cell code iPIC3D was developed by Markidis et al. (2010). The advantage of iPIC3D over explicit particle-in-cell codes is that iPIC3D is linearly unconditionally stable, so that iPIC3D can handle larger time step and larger cell size than explicit PIC codes. Compared to the explicit PIC method, the cell size of iPIC3D is chosen based on the scale of interest instead of the Debye length, and the time step of iPIC3D is not limited by the plasma frequency or the speed of light, but the accuracy condition, which requires $v_{\mathrm{RMS}}\Delta t/\Delta x < 1$ on all grid nodes for all species, where v_{RMS} is the root-mean-square of macroparticle velocities. In order to make the simulation as efficient as possible while keeping the accuracy condition satisfied, we implemented an adaptive time step scheme:

$$\Delta t = c_0 \cdot \min(\Delta x/v_{\mathrm{RMS}},\ \Delta y/v_{\mathrm{RMS}},\ \Delta z/v_{\mathrm{RMS}}), \tag{3}$$

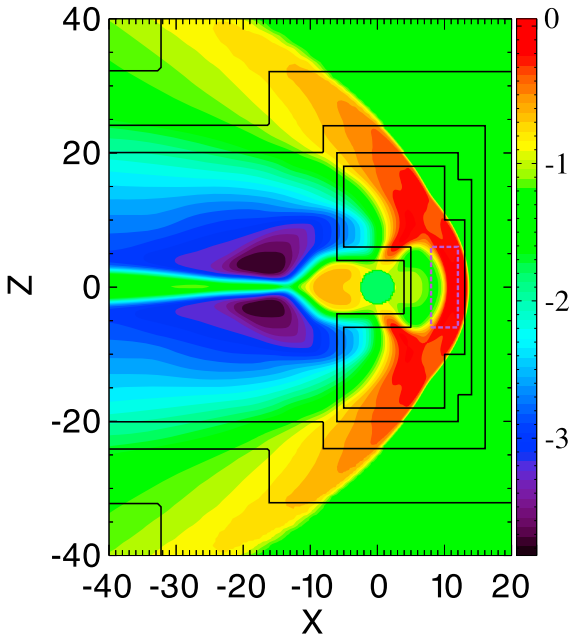

Figure 1. Part of the meridional plane with the adaptive MHD grid and the PIC region. The color represents the plasma pressure on a logarithmic scale. The black lines represent the refinement level, where the cell size changes. The resolution of the finest level around the dayside magnetopause is $1/16\,R_E$, and the refinement ratio between two nearby levels is 2. The dashed magenta box ($8\,R_E < x < 12\,R_E$, $-6\,R_E < z < 6\,R_E$) is the edge of the PIC region covered by iPIC3D, and it extends from $-6\,R_E$ to $6\,R_E$ in the y direction.

which is calculated for each grid node and the minimum is taken over the whole PIC mesh. The root-mean-square velocity v_{RMS} is similar to the thermal velocity but contains the effect of bulk velocity. c_0 is a coefficient that should be smaller than 1. $c_0 = 0.4$ is used for the simulation in this paper.

Since the focus of this paper is the dayside magnetopause reconnection, the embedded PIC box is placed near the subsolar magnetopause, where reconnection happens under purely southward IMF. In the GSM coordinates, the region inside $8\,R_E < x < 12\,R_E$ and $-6\,R_E < y, z < 6\,R_E$(see Figure 1) is solved by iPIC3D. The PIC region covers the magnetopause, and it is just inside the bow shock. The size of the ion diffusion region is the same order as the ion inertial length, and this kinetic scale should be resolved in order to capture reconnection kinetic physics. However, the ion inertial length $d_i = c/\omega_{pi}$ is about 60 km $\sim 1/100\,R_E$ for a typical magnetosheath density of 20 amu/cm^3. This length is so small that it is extremely difficult to resolve even for a 3-D global MHD model, not to mention the PIC code. Scaling up the kinetic length helps to reduce the required computational resources. In the present simulation, all the fluid values, including density, pressure, velocity, IMF, and dipole field strength, and also the derived values like the sound speed, Alfven velocity, and plasma beta, are realistic so that the global structure of the magnetosphere is comparable to the real system. On the other hand, the ion inertial length is scaled up 16 times to about $1/6\,R_E$ in the magnetosheath by artificially increasing ion mass per charge by a scaling factor of 16. Since all the quantities are normalized in the numerical model, there are several ways to understand or interpret the scaling. One way is treating the scaling as changing the charge of ions and electrons. Compared with the original system, we reduce the charge by a factor of 16 while all the other basic physical quantities, like mass per ion, number density, and temperature, remain realistic. From the perspective of ideal magnetohydrodynamics, the scaled system is exactly equivalent to the original one. For a particle-in-cell code, the reduction of charge per ion reduces the electromagnetic force on an ion and therefore increases the gyroradius and gyroperiod by a factor of 16. But the gyroradius and the gyroperiod are still several orders smaller than the global spatial and temporal scale, for example, the distance from Earth to the magnetopause and the time for the plasma moving from the subsolar point to the cusp, respectively. How the scaling changes the structure of reconnection is discussed in detail in our companion paper by Tóth et al. (2017). We also apply a reduced ion-electron mass ratio $m_i/m_e = 100$, which is sufficiently large to separate the electron and ion scales. We choose $\Delta x = 1/32\,R_E$ as the PIC grid resolution so that $d_i/\Delta x \sim 5$ and $d_e/\Delta x \sim 0.5$. This resolution keeps a balance between the computational cost and the requirement of resolving kinetic scales. Two hundred sixteen particles per cell per species are used, and there are about 9 billion particles in total inside the domain initially. Our numerical experiments suggest that smoothing the electric field **E** and the current density **j** can help to suppress the numerical noise (Tóth et al., 2017).

The typical magnetic field strength in the magnetosheath is about 30 nT, and the corresponding ion gyrofrequency is $\Omega_{ci} = 0.0286$ Hz and $\Omega_{ce} = 2.86$ Hz with scaled charge-mass ratio. As mentioned above, the time step of iPIC3D is determined by the accuracy condition (equation (3)). From the simulation, we find that the maximum thermal speed of electrons inside the PIC domain is about 2500 km/s, which leads to a time step of $\Delta t \sim 0.03s \sim 10^{-3}\Omega_{ci}^{-1} \sim 0.1\Omega_{ce}^{-1}$ with cell size $\Delta x = 1/32\,R_E$. Therefore, the time step is small enough to resolve the gyromotion of both electrons and ions.

2.3. Coupling Between BATS-R-US and iPIC3D

BATS-R-US and iPIC3D are coupled through the Space Weather Modeling Framework (SWMF). These two models are compiled together to generate a single executable file. Both models can run simultaneously on specified processors, and the information exchange is parallelized and handled by the Message Passing Interface. The details of the two-way coupling has been described by Daldorff et al. (2014).

In the simulation presented in this paper, we run the Hall MHD code first with the local time stepping scheme to reach a steady state. Then BATS-R-US sends the information, including density, velocity, pressure,

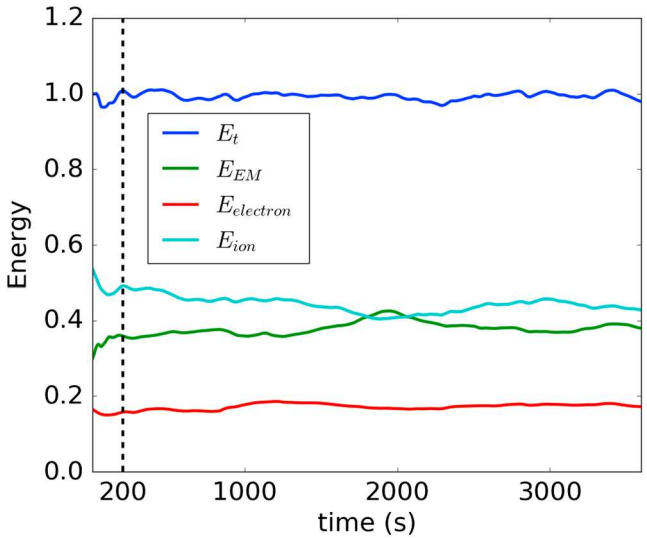

Figure 2. The normalized total energy E_t, electric field and magnetic field energy E_{EM}, ion energy E_{ion}, and electron energy $E_{electron}$. They are normalized by the initial total energy.

and magnetic field, to iPIC3D. iPIC3D initializes the electric field based on the Ohm's law. The Maxwellian-distributed particles are generated according to the fluid information so that iPIC3D and BATS-R-US have consistent density, velocity, and pressure at the same position. After the PIC initialization, the MHD and PIC models update independently with their own time steps. The coupling frequency between these two models can be set to a value that is independent of the MHD or PIC time step. During the coupling, iPIC3D calculates moments of the particle distribution function, such as the density, velocity, and pressure, and overwrites the MHD cells overlapping the PIC region. In return the MHD model provides electromagnetic field as well as particle boundary conditions for iPIC3D. For the particle boundary, iPIC3D removes the particles in the boundary cells and regenerates new particles based on the fluid variables obtained from MHD. Between the two coupling time points, iPIC3D uses the latest information obtained from BATS-R-US as a boundary condition during each iteration. In the simulation presented here, the time step for BATS-R-US and iPIC3D are around $\Delta t_{MHD} = 0.015$ s and $\Delta t_{PIC} = 0.032$ s, respectively. The MHD code and the PIC code are coupled every time step. The time step of PIC is larger than that of MHD because the MHD time step is limited near the magnetic poles due to the high Alfven speed, while these regions are outside the PIC domain.

Previously, we generated particles in only one ghost cell layer (Daldorff et al., 2014) as a particle boundary condition. Our numerical experiments suggested that using more layers (five layers specifically in this paper) as the particle boundary, while the electromagnetic field boundary is still only enforced at the outermost layer, is helpful to smoothly transit from PIC to MHD. The MHD cells overlapped with the PIC particle boundary are not overwritten by PIC. A similar technique has been used to implement open boundary condition for stand-alone PIC simulations (Peng et al., 2015).

We run the simulation on 6,400 processors for 170 h on Blue Water supercomputer (Bode et al., 2012) to model 1 h of simulation time. iPIC3D and BATS-R-US use about 80% and 15% of the simulation time, respectively. The coupling and other overhead use the remaining 5%.

2.4. Energy Conservation

Even though the PIC region is not a closed system, therefore mass and energy flow into and out of the region, it is still important to check the energy variation during the simulation to make sure the PIC model does not suffer from numerical heating or cooling. The normalized energy changes are shown in Figure 2. Throughout the simulation, the total energy E_t variation is less than 3%. The small variation suggests that the numerical heating or cooling are insignificant. The initial condition for iPIC3D is under MHD equilibrium but not necessarily under Vlasov equilibrium. The electromagnetic field energy E_{EM} and kinetic energy of each species normalized by the initial total energy are also shown in Figure 2. During the first several minutes, energy is transferred from the particles to the electromagnetic field. After 200 s, the ion and electron energy decrease about 5%, while the electromagnetic field energy increases from 0.3 to about 0.36. This is the transition from the MHD steady state to a PIC preferred state. Further change of these energies are gradual and small. E_{EM} is mainly magnetic field energy, which is about 3 orders larger than the electric field energy.

3. Results

3.1. Overview

The iPIC3D code is initialized from a steady Hall MHD state, which is shown in Figure 1. The steady state is obtained from the Hall MHD run by using a local time stepping scheme and a reconnection X line already exists near the equatorial plane along the dayside magnetopause. Since the local time stepping scheme is diffusive in this case, the reconnection signature near the X line is weak, for example, the Hall magnetic field strength is only about 1 nT. The PIC code inherits the magnetic field topology and starts evolving based on Maxwell's equations and the motion of the macroparticles. An overview of the evolution of the dayside magnetopause is shown in Figure 3, which contains the Hall magnetic field B_y and the field lines at the meridional plane inside the PIC box. At $t = 70$ s, B_y has already increased to about 8 nT. The Hall field extends far away

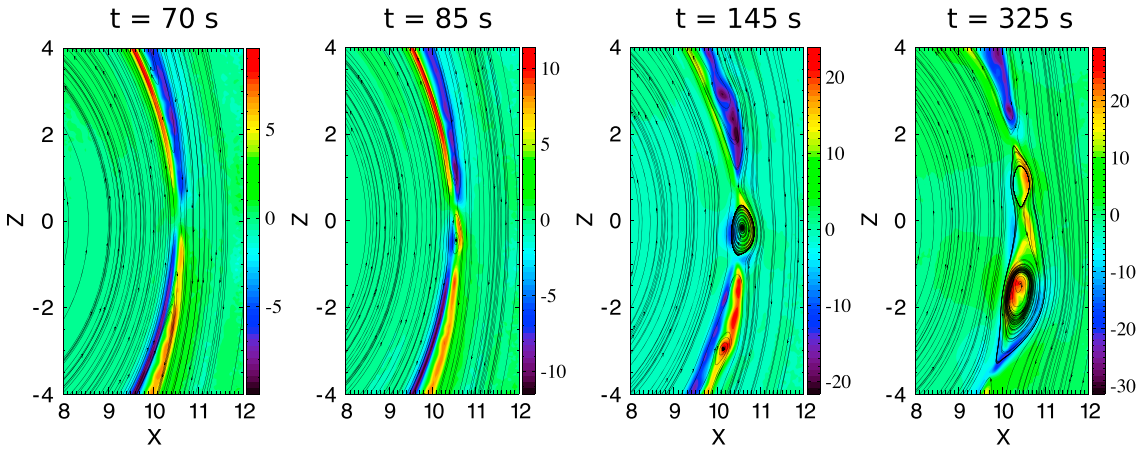

Figure 3. A series of snapshots showing B_y strength (color) and the projected magnetic field lines in the meridional plane inside the PIC region. The color bar is different in each plot.

from the X line with roughly the same field strength for each branch. Fifteen seconds later, south of the existing reconnection point, another X line starts to form at around $x = 10.2\,R_E$ and $z = -1\,R_E$. At $t = 145$ s, both X lines can be seen clearly, and a flux rope-like structure forms between the two X lines. The top X line has moved to about $z = 0.5$. The bottom X line is almost steady to this point, but it will move southward later. At $t = 325$ s, the top and bottom X lines reach about $z = 1.8$ and $z = -3.5$, respectively, and the center of the flux rope is moving southward with the bottom X line. Since the flux rope is moving away from the top X line, the current sheet between them becomes unstable and a secondary flux rope is generated (rightmost panel of Figure 3). During the 1 h simulation, flux ropes form near the subsolar point and move toward the poles quasi-periodically. More details about the reconnection and the flux ropes, for both macroscopic and microscopic scales, are discussed in the following subsections.

3.2. Evolution of FTEs

More complicated structures arise in 3-D. Flux ropes colored with the ion velocity z component u_{iz} at different times are shown in Figure 4. At $t = 100$ s, a short flux rope appears near the subsolar point. It is labeled as FTE-A. This flux rope extends from $y \sim -1\,R_E$ to $y \sim 1\,R_E$ in the dawn-dusk direction. It suggests that next to the primary X line near $z = 0$, another X line starts to form south of the subsolar point. We have checked a series of 2-D x-z plane cuts and found that the signature of reconnection, like the ion jets, at the second X line is clear at $y = 0$ but appears very weak far away from the Sun-Earth line, for example, at $y = 0.78\,R_E$ or $y = -0.78\,R_E$. At $t = 150$ s, the flux rope has extended significantly in both dawn and dusk directions. Along the flux rope, the ion velocity varies. Close to the duskside (positive y), the flux rope moves slowly, because the northward reconnection jet produced by the second X line slows down the southward flow originating from the primary X line. Close to the dawnside (negative y), the flux rope moves faster, because the reconnection at the second X line is not strong enough to significantly slow the southward flow ejected from the primary X line. The variation of the z component of the ion velocity along the flux rope, which is approximately aligned with the y direction, makes the flux rope inclined. At $t = 240$ s, the flux rope is even more tilted because of the varying ambient ion jet velocity. A new small flux rope, FTE-B in Figure 4, is generated at $t = 320$ s above FTE-A. FTE-A bifurcates at $y \sim -2.5$, and the new branch extends along the dawn-northward direction. FTE-A keeps moving southward while FTE-B is growing. At $t = 540$ s, a large portion of FTE-A, except for the dawn part, has already moved to the southern edge of the PIC domain ($z = -6$). FTE-B elongates significantly along the dawn-dusk direction. It is twisted at the dawnside so that the axial direction is almost parallel to the z axis. At the duskside, FTE-B connects to a newly formed flux rope FTE-C. At $t = 660$ s, FTE-B and FTE-C have merged and become indistinguishable. These 3-D plots suggest (1) flux ropes arise from multiple X line reconnection and can grow in time along the dawn-dusk direction, (2) the poleward moving velocity varies along a flux rope and makes them tilted, and (3) two flux ropes can merge and form a new long flux rope.

Since the PIC code is two-way coupled with the MHD model, the flux ropes can smoothly move out of the PIC region. Figure 5 shows a series of snapshots of j_y and field lines of FTE-A in the meridional plane (x-z plane) after it leaves the PIC domain. FTE-A moves southward along the magnetopause after being generated near

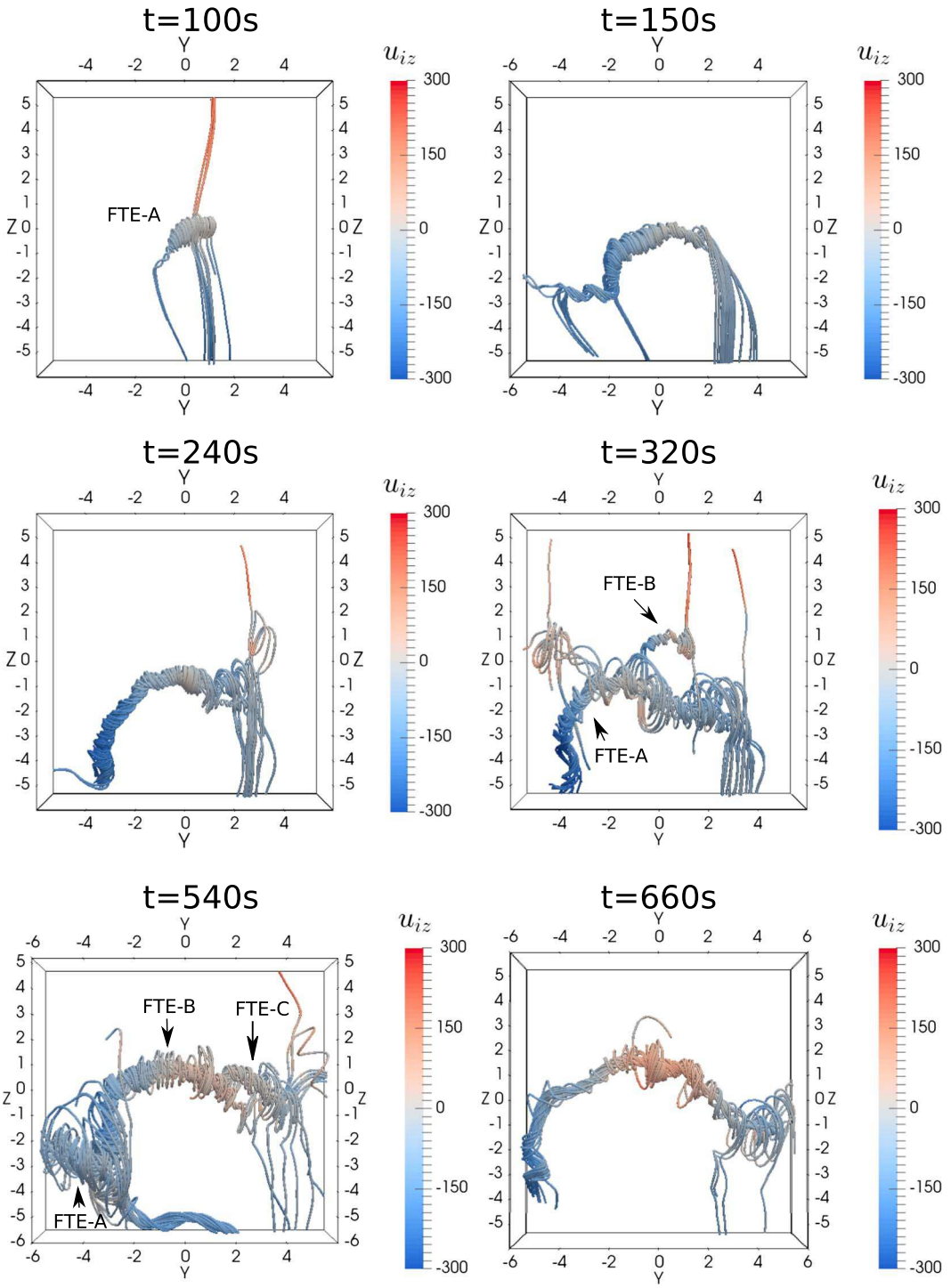

Figure 4. Evolution of FTEs. Viewed from the Sun, a series of snapshots are shown with magnetic field lines colored by ion velocity u_{iz}(km/s).

the subsolar point. At $t = 600$ s, the flux rope is already close to the southern cusp. There is strong axial current $j_y \sim 0.02\mu A/m^2$ near the center of the flux rope. As FTE-A moves toward the cusp, j_y inside the flux rope decreases in intensity, which indicates the dissipation of the magnetic helicity, as we can see at $t = 660$ s. When the FTE reaches the center of the cusp ($t = 720$ s), the field lines at the leading edge of the FTE and the cusp field lines are antiparallel and create a narrow and short current sheet with negative j_y around $x \sim 4\,R_E$ and $z \sim -9.5\,R_E$. The ion velocity u_{iz} at $x = 4\,R_E$ in Figure 6 shows a jump around $z = -9.5\,R_E$. The narrow

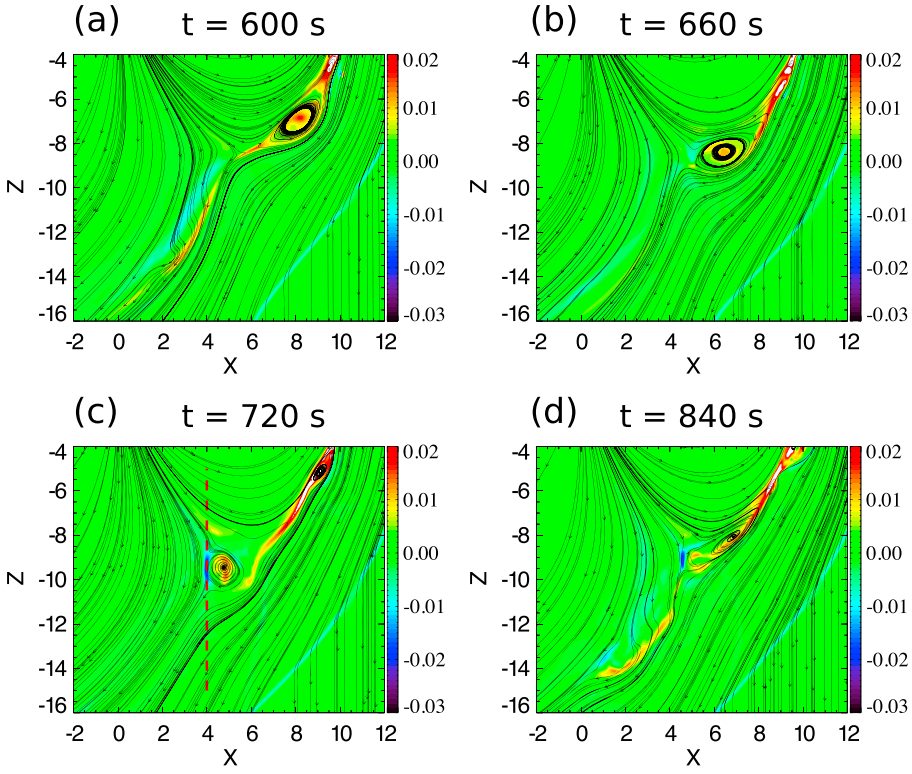

Figure 5. FTE dissipation crossing the southern cusp. A series of snapshots of current density $j_y(\mu A/m^2)$ and field lines are shown. The plots are obtained from MHD output. Along the FTE's trajectory, the grid is uniform and the cell size is $1/16\,R_E$. The red dashed line indicates the cut used in Figure 6.

current sheet and the velocity jump imply that reconnection occurs between the flux rope field lines and the cusp field lines. At $t = 840$ s, after FTE-A leaves the cusp, the signature of the flux rope becomes very weak: even though the magnetic field is still perturbed, the j_y component is close to zero near the center and no "O" line can be found. Finally, the remnant of the flux rope completely disappears as it moves toward the tail. Beside the FTE presented here, all other FTEs are also dissipated near the cusps in the meridional plane. Since an FTE is a 3-D structure, its behavior far from the meridional plane needs to be further explored. FTEs were observed by the satellite along the distant tail magnetopause ($x = -67\,R_E$) on the dusk flank (Eastwood et al., 2012). One possibility to explain the conflict between the simulation and the observation is that these FTEs may bypass the cusps and move along the flank from the dayside to the tail magnetopause.

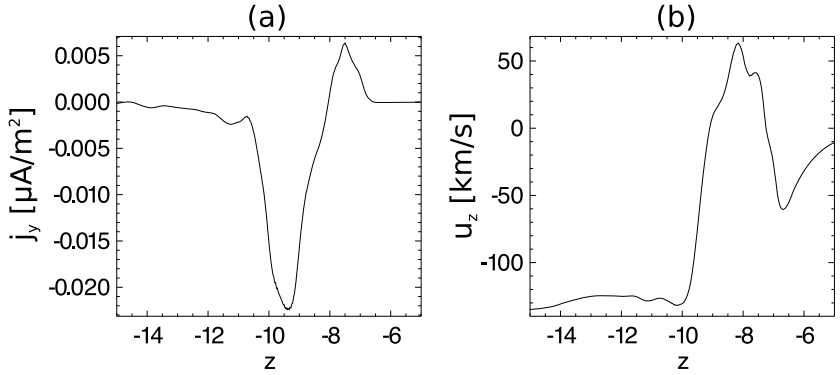

Figure 6. $j_y(\mu A/m^2)$ and u_z(km/s) along the vertical red dashed line marked in Figure 5c. The jump of u_z around $z \sim -9\,R_E$ implies the occurrence of magnetic reconnection.

3.3. Magnetic Field Signature

Since the most widely used indicator of FTEs in satellite data is the magnetic field signature, we discuss how the flux rope magnetic field looks like along a virtual satellite trajectory. A series of meridional cuts are shown in Figure 7 to illustrate the magnetic field evolution. At $t = 290$ s, north of the FTE-A event, there is an X line at about $z = 1\,R_E$ surrounded by the quadrupolar Hall magnetic field B_y. As expected, the two branches on the magnetosheath side with amplitude of ~30 nT are stronger than the other two on the magnetosphere side with amplitude of ~10 nT. Near the X line, the magnetosheath and magnetosphere are separated by a current sheet with very weak magnetic field. Thirty seconds later, another X line near $z = 0$ arises, and an O line forms between the two X lines. Around the edge of the O lines, the azimuthal component of the magnetic field grows, while the B_y component is still very weak just near the center. We note that the strong field on the magnetosheath side of the flux rope is mainly contributed by the B_z component because of the accumulation of the inflow of magnetic flux. The reconnection at the northern X line is stronger than that of the southern one, so the ion jet around the O line is moving southward with a slow speed less than 100 km/s. Inside the O line, the pressure starts increasing. One hundred seconds later, the pressure at the center of the flux rope has reached about 1.3 nPa while the core field is still small. At $t = 540$ s, the O line structure continues to grow as the two X lines move northward and southward, respectively. We can see the core field B_y at the center of the O line has grown to a significant value of ~30 nT now, while the center pressure drops to ~1.0 nPa. The converging jets from the two X lines are comparable, and the flux rope is almost steady. One hundred eighty seconds later, the core field grows to ~ 40 nT and the corresponding pressure drops to about 0.8 nPa. The whole structure at this stage is moving northward driven by the ion jet generated by the southern X line. To demonstrate the scaling factor has weak influence on the global structures, we performed another simulation with ion inertial length increased by a factor of 32. The simulation results are shown in Figure 8. The FTE in Figure 8 develops similar to the one in Figure 7: the core field grows gradually and the ion pressure is anticorrelated with the core field strength. The FTEs in Figures 8 and 7 also have comparable sizes.

At the early time when the O line just formed, for example, at $t = 420$ s, the weak core field is surrounded by relatively large toroidal fields. We argue that this is an example of the so-called "crater FTEs" that have been observed by spacecrafts (LaBelle et al., 1987; Zhang et al., 2010). Since the O line moves slowly during its initial stage of formation, the magnetic field observed at a fixed point cannot reflect its global structure. Instead, the magnetic field along the magnetopause (the red curve in Figure 9a) is shown in Figure 9a to illustrate its magnetic field structure. Along the magnetopause, from south to north, the B_x field, which is roughly normal to the magnetopause, reaches a local minimum of ~ −15 nT at $z = 0$ and then quickly increases to ~15 nT at $z = 1\,R_E$. The flux rope is bounded by the depressed magnetic field "trenches" at $z = -0.2\,R_E$ and $z = 2\,R_E$ as indicated by B_t. The depression results from the low magnetic field strength inside the current sheet as can be seen from Figures 9c and 9e. B_t reaches a local maximum at the same position of the B_x peaks ($z = 0\,R_E$ and $z = 1\,R_E$), while the field strength decreases to about 10 nT between the peaks. We refer to the event on 30 July 2007 observed and analyzed by Zhang et al. (2010) for comparison. Figure 6 of Zhang et al. (2010) shows the magnetic field signature of this event. Even though the 30 July 2007 event has a large guide field (corresponding to B_y component in our simulation), and its magnetic field around the flux rope is more steady than our simulation, the whole structure of this event is similar to what is shown in Figure 9.

As the flux rope evolves, the core field strength grows to a significant value. The magnetic field measured at a fixed position $x = 10.2\,R_E$, $z = 2.75\,R_E$ is shown in Figures 10c and 10e. The vertical dashed line at $t = 760$ s represents the location of the maximum B_t. Around this time, the B_x field, which is roughly perpendicular to the magnetopause, jumps from ~ 5 nT to ~ −20 nT within about 25 s. At $t = 760$ s, both the axial field B_y and the total field B_t reach a maximum. These features match the signatures of the FTE observed by Zhang et al. (2010). During the 1 h long simulation, there are 10 FTEs with significant core field moving across the southern PIC edge. The occurrence frequency is consistent with observations (Rijnbeek et al., 1984) and previous MHD simulations (Raeder, 2006).

The IMF is purely southward in our simulation and there is no uniform background guide field at the magnetopause. But a significant core field can still arise during the FTE generation and evolution as seen in Figure 7. When a flux rope is still close to the X lines, the core field may be encompassed by the Hall magnetic field generated by the reconnection, resulting in complicated guide field structure. The B_M field at $t = 540$ s is shown in Figure 11. In order to compare with observations, the magnetic field has been transformed into a boundary normal coordinate system (**LMN**), in which the **N** component points outward, normal to the magnetopause,

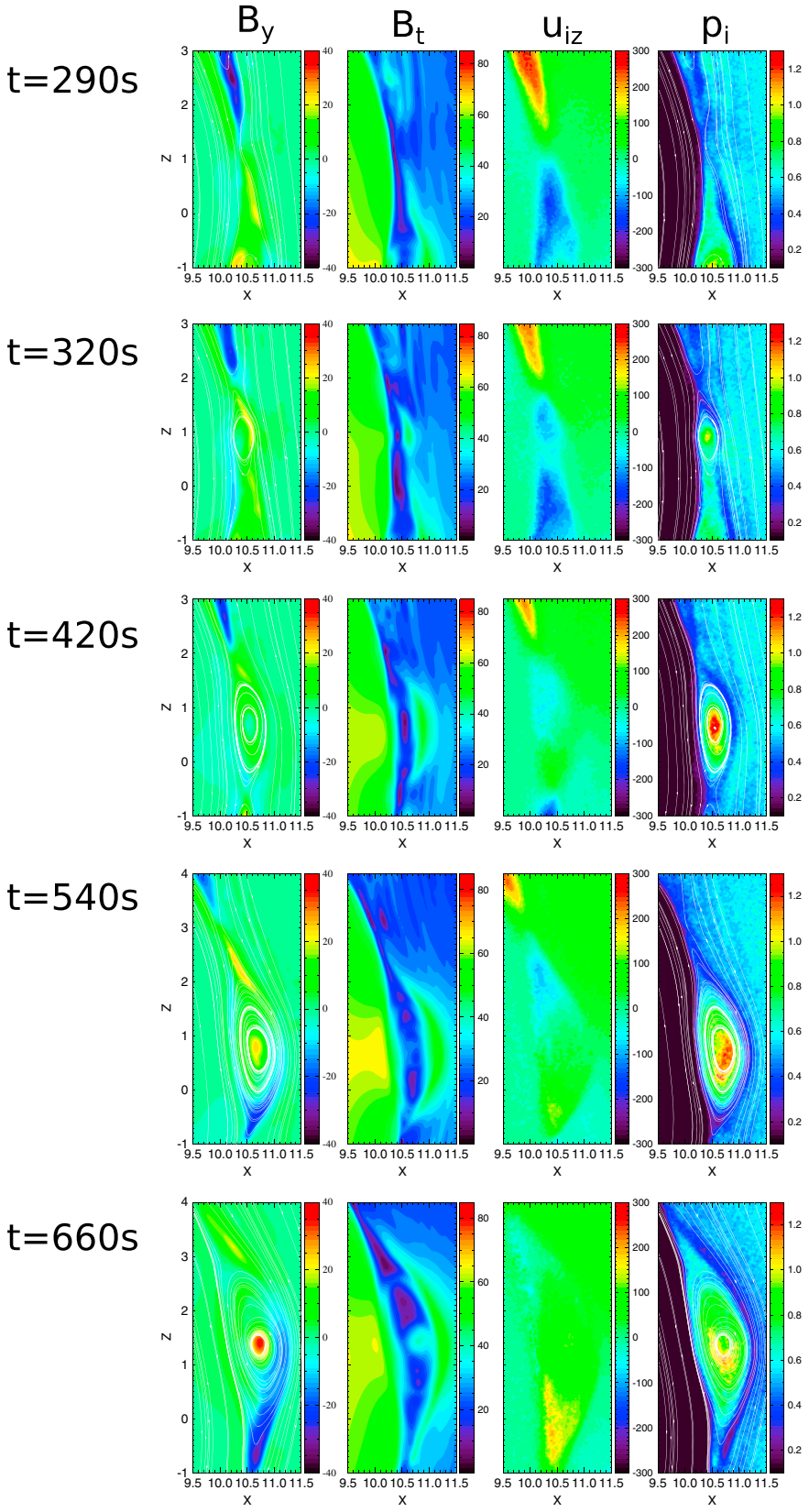

Figure 7. The evolution of FTEs in the meridional plane. (left to right) The four columns show the B_y(nT) and the projected magnetic field lines; the field strength B_t(nT); the ion velocity in z direction U_{iz}(km/s); and the ion pressure p_i(nPa) overlapped with magnetic field lines.

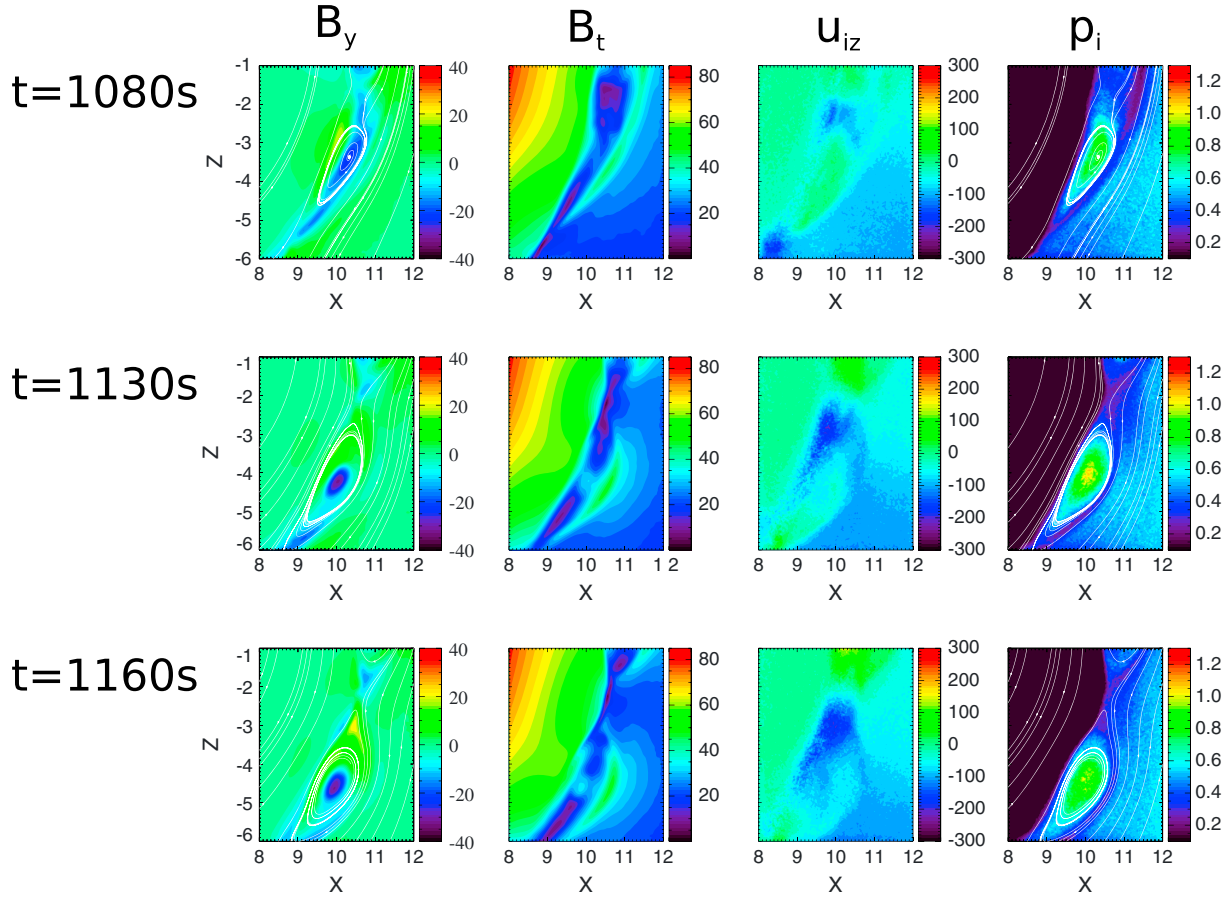

Figure 8. Same as Figure 7 except that the ion inertial length is scaled up by a factor of 32.

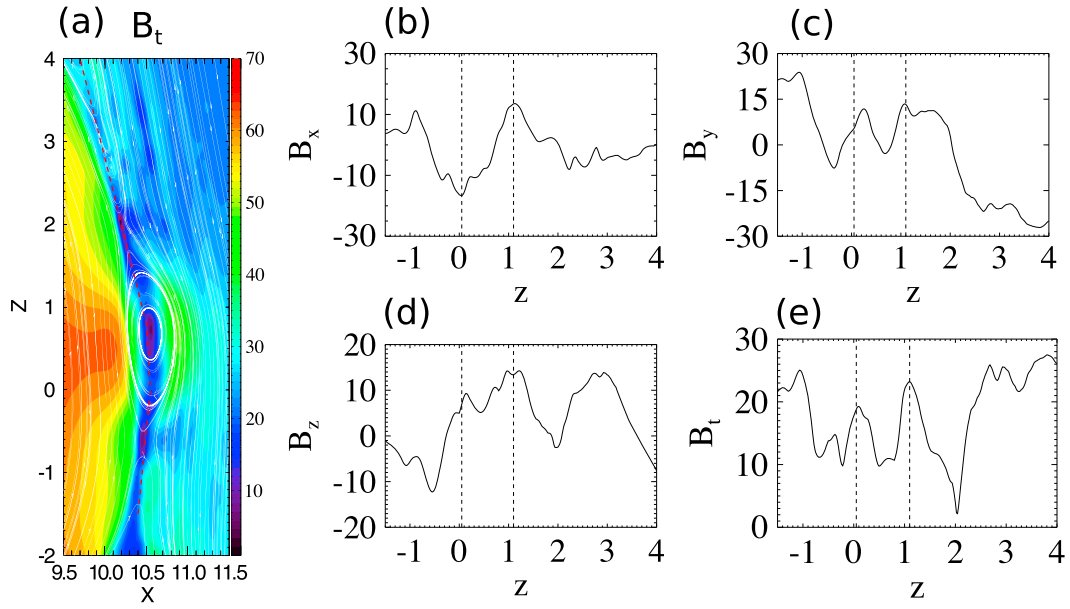

Figure 9. The crater flux rope at t = 420 s. (a) The magnetic field strength and field lines. (b–e) The magnetic field along the red dashed line in Figure 9a. The two vertical dashed lines represent the two peaks of B_x.

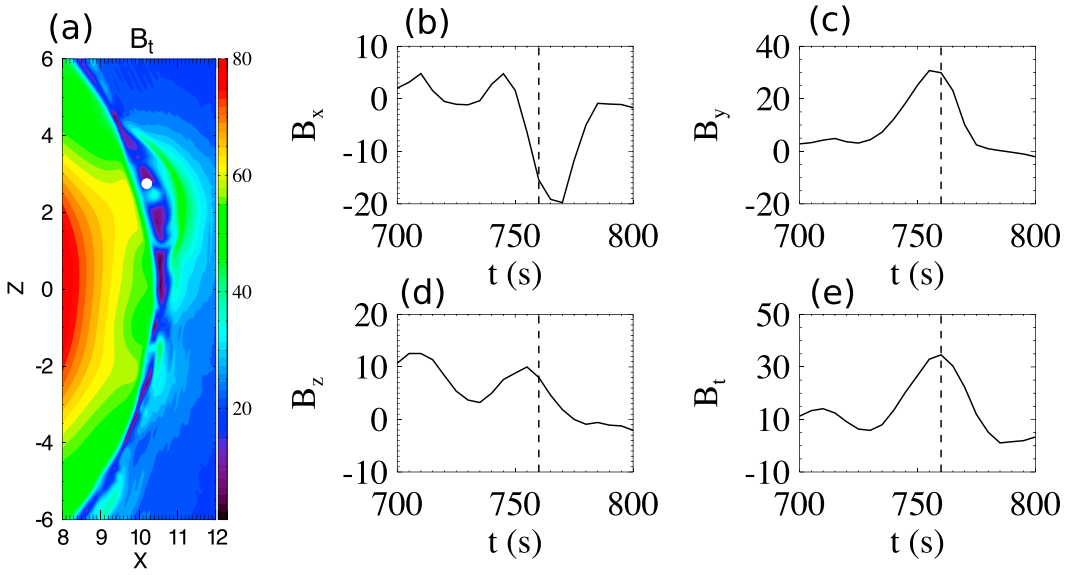

Figure 10. The magnetic field signature of a flux rope with significant core field. (a) The magnetic field strength at $t = 740$ s. The white filled circle at $x = 10.2\,R_E$, $z = 2.75\,R_E$ is the location of the fixed virtual satellite. (b–e) The magnetic field observed by the satellite. The vertical dashed line at $t = 760$ s indicates the location of maximum B_t.

the **M** component is determined by $\mathbf{N} \times \mathbf{Z}_{GSM}$, and the **L** component completes the right-hand coordinate system. Since the plot is shown in the meridional plane, the $\mathbf{Y}_{GSM}$ direction is antiparallel to the **M** direction. Around the flux rope center, the guide field B_M is negative, while the southern part of this flux rope is surrounded by positive B_M. The polarity of the positive "*Y*" shape B_M is consistent with the Hall magnetic field generated by the X line at $z = -1\,R_E$. If a satellite is moving across the flux rope along the red solid line in Figure 11a, the satellite will observe a tripolar guide field structure (Figure 11b). Similar structure was first observed in the solar wind (Eriksson et al., 2015), and it was also observed by the Polar satellite at the magnetopause (see Eriksson et al., 2016, Figure 1). The Polar event shows a large negative B_M core field bounded by two narrow B_M depressions in the presence of a large background guide field. There is no background guide field in our simulation, and thus Figure 11b shows a pure tripolar structure: the large negative B_M field is surrounded by two relative small positive peaks. Despite the difference in the background guide field, the topology of B_M obtained from our simulation is very similar to the Polar observation.

3.4. Kinetic Features

We have examined the global structure of the FTEs in the previous discussion. In this subsection, we will demonstrate that the underlying kinetic physics is properly captured by our model. The Larmor electric field, identified by Malakit et al. (2013), is a localized electric field that appears on the magnetospheric side of the dayside reconnection site. The *x* component of the electric field E_x at the end of the simulation (t =3,600 s) is shown in Figure 12. The positive E_x pointing toward the Sun along the magnetopause is the Hall electric field, while behind the Hall electric field, the localized negative field pointing toward the Earth is the Larmor electric field. A 1-D cut through the reconnection site along the *x* direction is also shown in Figure 12. The Larmor field strength is −3 mV/m, the magnetospheric side ambient field is about 2 mV/m, and the nearby Hall field is about 12 mV/m. These values are reasonably close to the MMS observation by Graham et al. (2016), for which the Hall electric field strength was ∼ 20 mV/m and the Larmor field strength was about 10 mV/m (see Graham et al., 2016, Figure 2).

Even though the ion inertial length is scaled up by a factor of 16 in the present simulation, the electric field strength is not sensitive to the scaling factor. Ignoring the electron inertia term, the generalized Ohm's is

$$\mathbf{E} = -\mathbf{u_i} \times \mathbf{B} + \frac{1}{q_i n_i}\mathbf{j} \times \mathbf{B} - \frac{1}{q_i n_i}\nabla p_e = -\mathbf{u_e} \times \mathbf{B} - \frac{1}{q_i n_i}\nabla p_e \tag{4}$$

Tóth et al. (2017) show the electron velocity $\mathbf{u_e}$ of the current sheet does not change with the scaling factor while the current sheet width scales. The gradient of electron pressure is inversely proportional to the scaling factor, because the pressure jump is fixed across the current sheet and the current sheet width is proportional

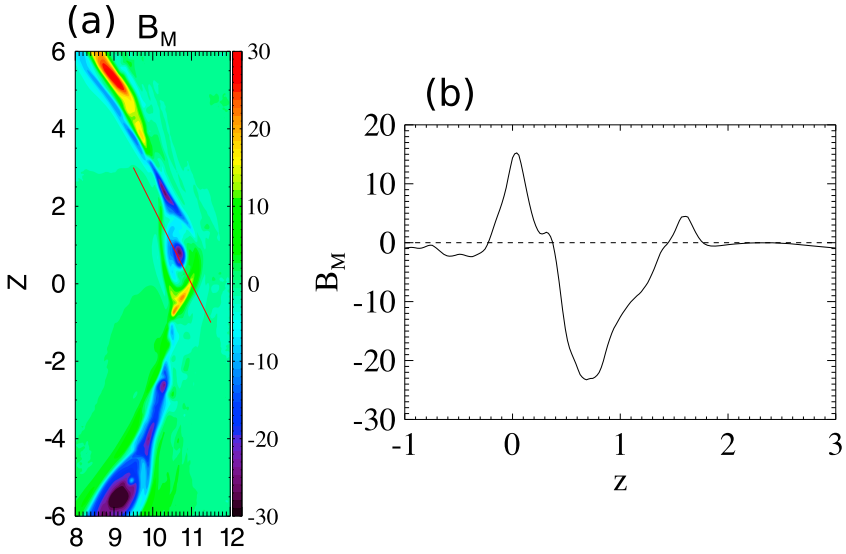

Figure 11. The tripolar guide field structure. (a) The B_M component in the meridional plane at $t = 540$ s. Around the flux rope center, the guide field is negative, while the southern part of this flux rope is surrounded by the "Y" shaped positive B_M. The field along the red solid line is shown in Figure 11a.

to the scaling factor. Since the charge per ion or electron is also reduced by the same factor, the scaling does not change the electric field strength. Besides the scaling of the ion inertial length, a reduced ion-electron mass ratio $m_i/m_e = 100$ is used in this study to increase electron kinetic scales (see section 2.2). The influence of the mass ratio m_i/m_e has been studied in numerous papers (Hesse et al., 1999; Lapenta et al., 2010; Ricci et al., 2004; Shay & Drake, 1998; Shay et al., 2007). For the Larmor electric field, Malakit et al. (2013) specifically estimates its amplitude to be

$$E \sim \frac{k_B T_i}{q_i r_i}, \tag{5}$$

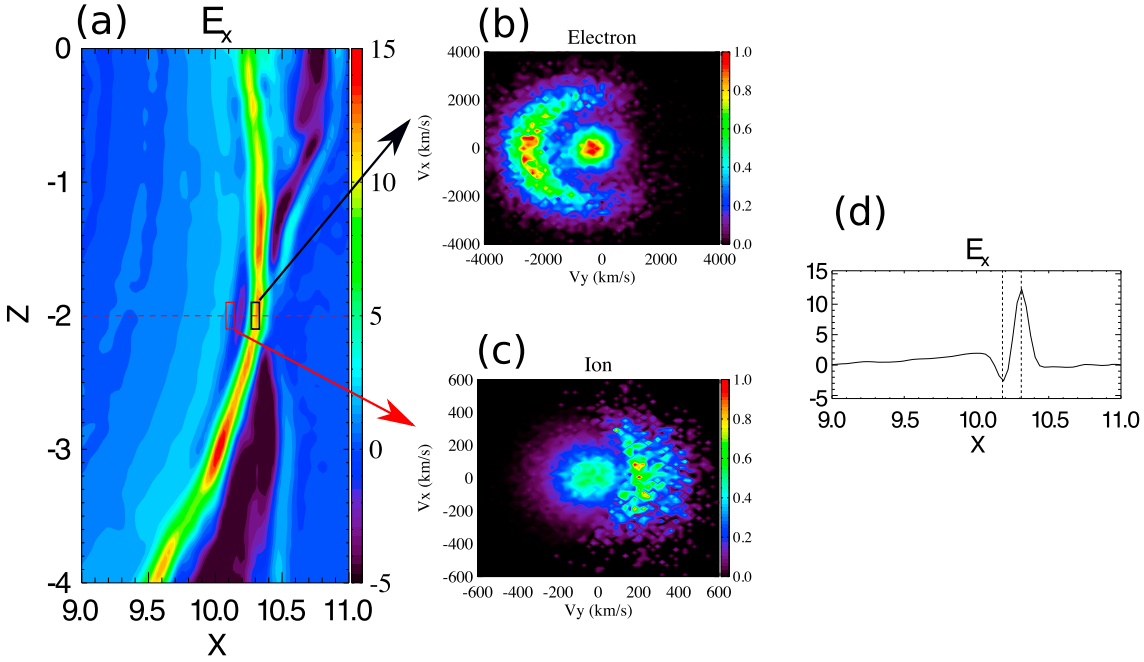

Figure 12. The Larmor electric field and crescent electron and ion phase space distributions. (a) E_x(mV/m) in the meridional plane at $t = 3,600$ s. (b) The normalized electron distribution in $V_y - V_x$ phase space. The electrons are inside the black box shown in Figure 12a: $10.27\,R_E < x < 10.33\,R_E$, $-0.3\,R_E < y < 0.3\,R_E$, and $-2.1\,R_E < z < -1.9\,R_E$. (c) Ion phase space distribution for particles inside the red box in Figure 12a: $10.08\,R_E < x < 10.14\,R_E$, $-0.3\,R_E < y < 0.3\,R_E$, and $-2.1\,R_E < z < -1.9\,R_E$. The phase density is normalized. (d) E_x along the red dashed line in Figure 12a.

where k_B is the Boltzmann's constant, T_i, q_i, and r_i are the temperature, charge per ion, and ion Larmor radius of the ions on the magnetospheric side. In the simulation, q_i is reduced by a factor of 16 and r_i becomes 16 times larger compared to the realistic situation, while the temperature T_i does not change. So, the scaling of inertial length should not influence the strength of the Larmor electric field. On the magnetosheath side, our simulation shows the ion temperature is about 2×10^6 K, and the magnetic field strength is about 60 nT. Substituting these values into equation (5) gives $E \sim 5.5$ nT. As mentioned above, the value obtained from simulation is about −3 mV/m.

The crescent shape electron phase space distribution has been observed near the electron diffusion region at the dayside magnetopause by MMS (Burch et al., 2016). The same distribution is also found in our 3-D global simulation. The phase space distribution of electrons inside a cube region: $10.27\,R_E < x < 10.33\,R_E$, $-0.3\,R_E < y < 0.3\,R_E$, and $-2.1\,R_E < z < -1.9\,R_E$is shown in Figure 12. The crescent distribution is found in the $V_y - V_x$ plane, corresponding to the two velocity components perpendicular to the magnetic field. The crescent hot electrons are drifting along negative y direction with a speed close to 3,000 km/s. The direction of the flow is consistent with the $\mathbf{E} \times \mathbf{B}$ direction, and the velocity of the crescent particles is very close to the MMS observation (Burch et al., 2016). Slightly farther away from the reconnection site, where the Larmor field appears, inside a cube $10.08\,R_E < x < 10.14\,R_E$, $-0.3\,R_E < y < 0.3\,R_E$, and $-2.1\,R_E < z < -1.9\,R_E$, the ion phase space distribution also presents crescent-like shape as it is shown in Figure 12c. The crescent ions drift in positive y direction because E_x is negative. We also checked the distributions for particles inside the current sheet but far from the reconnection site, and no crescent distributions are found for either electrons or ions.

Kinetic effects along the magnetopause current direction are also captured by our 3-D MHD-EPIC model. Figure 13 shows the fully developed lower hybrid drift instability (LHDI) at the end of the simulation ($t = 3,600$ s) at the $z = -3\,R_E$ plane. The electric field E_M shown in Figure 13 is the **M** component in the boundary normal coordinates, and **M** is antiparallel to the current direction. The black curve in Figure 13 separates the negative and positive B_z. We can see the LHDI appears along the magnetopause on the magnetospheric side. A closer view of E_M, as well as B_z, ion mass density ρ_i, and electron velocity u_{ey}, is also shown Figure 13. The LHDI arises near the interface of magnetosheath and magnetosphere, where there is a sharp density gradient. B_z, ρ_i, and u_{ey} show sawtooth pattern at the same location. The amplitude of the LHDI electric field is about 8 mV/m, which is consistent with MMS observations (Graham et al., 2016). The dominant wavelength shown in Figure 13b is about $0.38\,R_E$, and the ambient magnetosheath side electron gyroradius is about $r_e = 0.025\,R_E$ with the artificially changed charge per electron mass ratio, which results in $kr_e \sim 0.4$, where $r_e = m_e v_e/(q_e B)$ and v_e is defined as $v_e = \sqrt{2T_e/m_e}$. The value of kr_e is also consistent with observations (Graham et al., 2016) and theory (Daughton, 2003). We analyzed the LHDI at different times and different locations; the value of kr_e varied from ~ 0.3 to ~ 0.5, and $kr_e \sim 0.4$ is a typical value. Similar to the argument above with the Ohm's law, the electric field strength is not sensitive to the scaling; that is why the LHDI electric field strength agrees with MMS observations. But the length scale does change with the scaling. The charge per mass of electron q_e/m_e is artificially increased by a factor of 294 in the simulation, and the electron thermal velocity is reduced by a factor of $\sqrt{18.36} = 4.3$ for $m_i/m_e = 100$. The magnetic field is realistic; hence, the electron gyroradius is about 68 times larger than in reality. If we scale back the LHDI wavelength of the simulation by the same factor, it will be ~ 35 km. As a comparison, MMS observed 10 km to 13 km wavelength (Graham et al., 2016). Figure 13f shows the isosurfaces of $E_M = 4$ mV/m colored by the ion velocity u_{iz} viewed from the Sun. Along the magnetic field direction, the isosurfaces are cut off 2 or 3 times. The ion velocity jumps or even changes directions across a cutoff region. It suggests that these cutoff regions correspond to reconnection sites and that the LHDI electric field is weak near the diffusion regions (Pritchett, 2013).

3.5. Comparison With Hall MHD

For comparison, we also run a pure Hall MHD simulation with the same setup except the PIC region is removed and the MHD grid resolution around the dayside magnetopause is refined to $1/32\,R_E$, which is the resolution used by PIC in the MHD-EPIC run. Even for Hall MHD, resolving the ion inertial length is necessary in order to capture the Hall effect correctly. Due to the small kinetic scale inside the magnetosheath, scaling the ion inertial length is also required for a global Hall MHD simulation since Hall MHD is also computationally expensive as we will see. We note that the ion inertial length in the pure Hall MHD simulation is also scaled up by a factor of 16 so it can be resolved with the $1/32\,R_E$ cell size. Hall MHD is reasonably optimized by using a semi-implicit scheme to overcome the time step imposed by the whistler mode wave and speed up the simulation. It still takes 6,400 cores running about 67 h to model 1 h because of the high resolution and the stiffness of the Hall term. As a comparison, the MHD-EPIC simulation (170 h on 6,400 cores) is about 2.5 times more expensive.

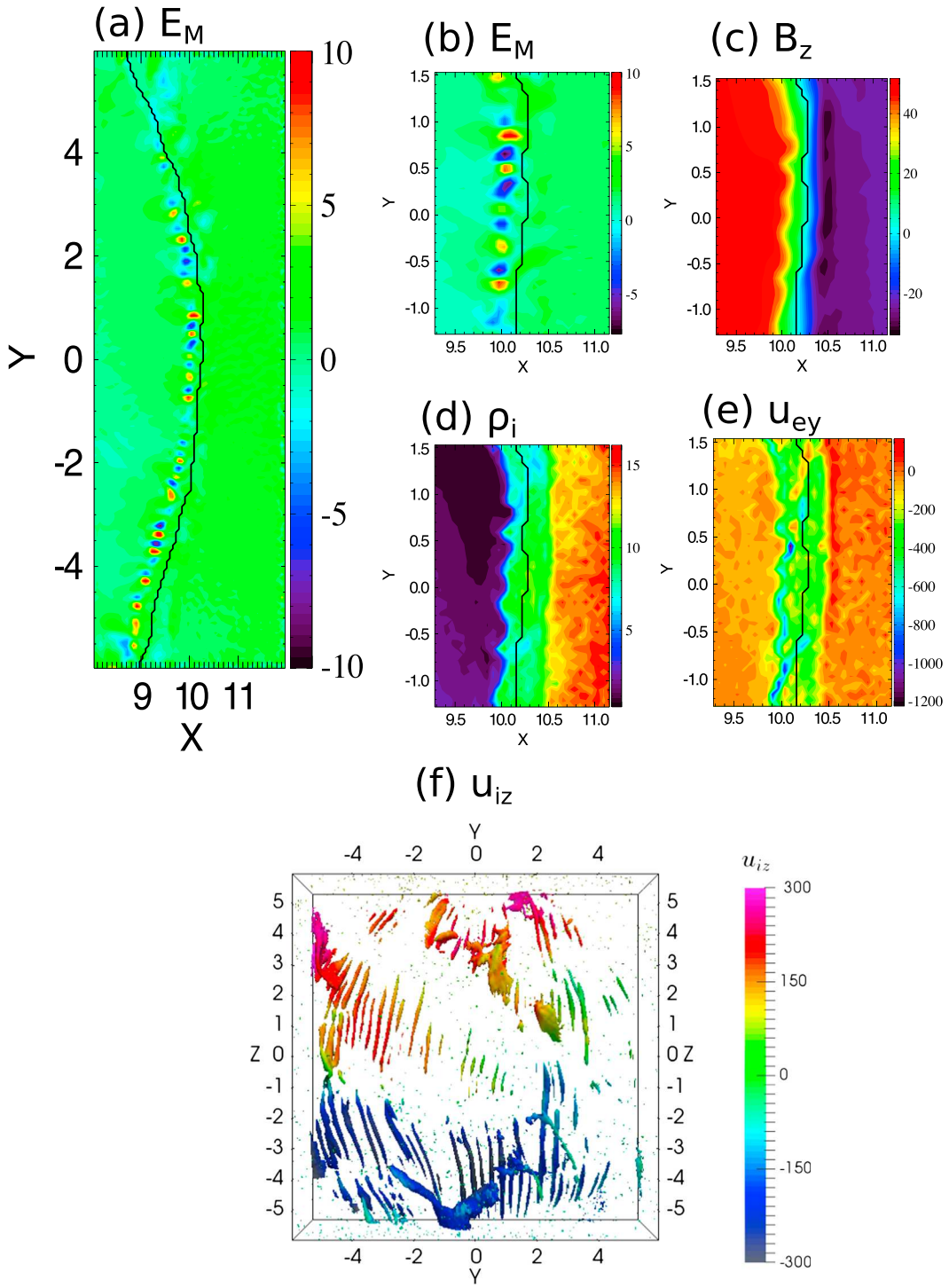

Figure 13. The lower hybrid drift instability (LHDI) at $t = 3600$ s. (a) Electric field E_M(mV/m) along the direction that is antiparallel to the magnetopause current direction in the $z = -3\,R_E$ plane. Near $y = 0$, the current direction is almost parallel to the y direction. (b–e) Zoomed in view of different variables for LHDI at $z = -3\,R_E$. (c) The B_z field in nanotesla. (d) The ion density in amu/cm^3. (e) The electron velocity along y direction. The black curves in Figures 13a–13e separate the negative and positive B_z. (f) The 3-D contour surface of $E_M = 4$ mV/m colored by the ion velocity along the z direction (u_{iz}(km/s)).

Hall MHD produces the Hall magnetic field near the X line and generates flux ropes in a way similar to MHD-EPIC. But Hall MHD cannot reproduce the kinetic features, neither the crescent particle distributions nor the LHDI.

4. Summary and Conclusion

We have performed a 1 h long high-resolution global simulation with the MHD-EPIC model to study dayside reconnection and FTEs. Our simulation is the first attempt to investigate the FTEs and reconnection with kinetic physics resolved in a realistic magnetopause environment. Although the kinetic scale is artificially increased to reduce the computational cost, the model still captures the kinetic features very well. MMS observations, like the crescent particle phase space distribution and LHDI, are reproduced in our model. The FTEs from the simulation also agree well with spacecraft observations. The key results from the present simulation are as follows.

1. When an FTE arises, its cross section is small and it is short in the dawn-dusk direction. During its growth, the cross section increases and the FTE extends along the dawn-dusk direction.
2. An FTE forms near the subsolar point and moves toward the poles under steady southward IMF conditions. When the FTE reaches the cusp, reconnection happens between the FTE magnetic field and the cusp magnetic field lines, thus dissipating the FTE. The signature of the FTE in the meridional plane is weak behind the cusps.
3. An FTE is flanked by two reconnection sites during its formation, and the converging ion jets are found around the FTE.
4. The present simulation confirms that the "crater FTEs" magnetic field signature can be found at the early stage of an FTE formation when the axial magnetic field is still weak. A strong core field may develop as the FTE evolves, and the Hall magnetic field may provide the initial seed core field. Therefore, a fully developed FTE has the typical strong core field structure.
5. A tripolar guide field structure is found from our simulation.
6. The Larmor electric field is found near the reconnection site on the magnetospheric side, and its amplitude is about −3 mV/m.
7. A crescent electron phase space distribution is found near the reconnection site where the Hall electric field reaches its maximum. A similar distribution is also found for ions at the place where the Larmor electric field appears.
8. The lower hybrid drift instability (LHDI) appears at the interface of the magnetosheath plasma and magnetosphere plasma. The LHDI electric field peak strength is about 8 mV/m, and a typical ratio between its wavelength and the electron gyroradius is about $kr_e \sim 0.4$. The simulation agrees with the MMS observations and theory.

Compared to the models relying on ad hoc resistivity or numerical resistivity to generate FTEs or investigate reconnection process, our 3-D MHD-EPIC model makes one significant step forward by incorporating a self-consistent kinetic description of reconnection into a global MHD model. While the kinetic scales are increased by artificially reducing the charge per mass for both ions and electrons, all the other parameters are realistic. The scaling changes the size of kinetic features, for example, the wavelength of LHDI, but other values, like the strength of Larmor electric field or LHDI electric field, are not modified by the scaling. Another artificial change is the solar wind electron pressure. It is set to a value 8 times larger than the ion pressure so that $p/p_e \sim 2.5$ inside the magnetosheath while the ratio is usually about 4 to 12 from observation (Wang et al., 2012). The artificially increased electron pressure can help to stabilize the simulation, and it does not deviate significantly from the observed values. We plan to improve this in the future studies.

The MHD-EPIC model offers a powerful tool to study magnetospheric physics. The PIC code only covers the dayside magnetopause in the present simulation. As a natural extension, it can be elongated to cover the bow shock so that the kinetic processes associated with the bow shock can be modeled. Another future application is covering the tail reconnection site with another PIC region, so that both dayside and tail reconnections are handled by a kinetic code. Then we will be able to study substorm in a more realistic way. Both the ion pressure and electron pressure are solved by the MHD code in the current simulation, but they are scalars. The missing of the off-diagonal pressure tensors introduces discrepancy at the boundaries of the PIC code. This discrepancy can be improved by using a 10-moment fluid model in the future.

Acknowledgments
This work was supported by the INSPIRE NSF grant PHY-1513379, NSF strategic capability grant AGS-1322543, NASA grant NNX16AF75G, NASA grant NNX16AG76G, and the Space Hazards Induced near Earth by Large, Dynamic Storms (SHIELDS), and the Impacts of Extreme Space Weather Events on Power Grid Infrastructure projects funded by the U.S. Department of EnergyDE-AC52-06NA25396 through the Los Alamos National Laboratory Directed Research and Development program. Computational resources supporting this work were provided on the Blue Waters supercomputer by the NSF PRAC grant ACI-1640510, on the Pleiades computer by NASA High-End Computing (HEC) Program through the NASA Advanced Supercomputing (NAS) Division at Ames Research Center, and from Yellowstone (ark:/85065/d7wd3xhc) provided by NCAR's Computational and Information Systems Laboratory, sponsored by the National Science Foundation. The SWMF code (including BATS-R-US and iPIC3D) is publicly available through the csem.engin.umich.edu/tools/swmf website after registration. The output of the simulations presented in this paper can be obtained by contacting the first author Yuxi Chen.

References

Bessho, N., Chen, L.-J., & Hesse, M. (2016). Electron distribution functions in the diffusion region of asymmetric magnetic reconnection. *Geophysical Research Letters*, *43*, 1828–1836. https://doi.org/10.1002/2016GL067886

Bode, B., Butler, M., Dunning, T., Gropp, W., Hoe-fler, T., Hwu, W.-M., & Kramer, W. (2012). The Blue Waters super-system for super-science. Contemporary HPC Architectures, Jeffery Vetter eds., Sitka Publications. Boca Raton, FL: CRC Press. http://science.sciencemag.org/content/352/6290/aaf2939

Burch, J. L., Torbert, R. B., Phan, T. D., Chen, L.-J., Moore, T. E., Ergun, R. E., … Chandler, M. (2016). Electron-scale measurements of magnetic reconnection in space. *Science*, *352*(6290).

Daldorff, L. K. S., Tóth, G., Gombosi, T. I., Lapenta, G., Amaya, J., Markidis, S., & Brackbill, J. U. (2014). Two-way coupling of a global Hall magnetohydrodynamics model with a local implicit particle-in-cell model. *Journal of Computational Physics*, *268*, 236–254. https://doi.org/10.1016/j.jcp.2014.03.009

Daly, P. W., Williams, D. J., Russell, C. T., & Keppler, E. (1981). Particle signature of magnetic flux transfer events at the magnetopause. *Journal of Geophysical Research*, *86*(A3), 1628–1632.

Daughton, W. (2003). Electromagnetic properties of the lower-hybrid drift instability in a thin current sheet. *Physics of Plasmas*, *10*(8), 3103–3119.

Dorelli, J. C., & Bhattacharjee, A. (2009). On the generation and topology of flux transfer events. *Journal of Geophysical Research*, *114*, A06213. https://doi.org/10.1029/2008JA013410

Eastwood, J. P., Phan, T. D., Cassak, P. A., Gershman, D. J., Haggerty, C., Malakit, K., … Wang, S. (2016). Ion-scale secondary flux ropes generated by magnetopause reconnection as resolved by MMS. *Geophysical Research Letters*, *43*, 4716–4724. https://doi.org/10.1002/2016GL068747

Eastwood, J. P., Phan, T. D., Fear, R. C., Sibeck, D. G., Angelopoulos, V., Øieroset, M., & Shay, M. A. (2012). Survival of flux transfer event (FTE) flux ropes far along the tail magnetopause. *Journal of Geophysical Research*, *117*, A08222. https://doi.org/10.1029/2012JA017722

Eriksson, S., Cassak, P. A., Retinò, A., & Mozer, F. S. (2016). Subsolar magnetopause observation and kinetic simulation of a tripolar guide magnetic field perturbation consistent with a magnetic island. *Geophysical Research Letters*, *43*, 3035–3041. https://doi.org/10.1002/2016GL068691

Eriksson, S., Lapenta, G., Newman, D. L., Phan, T. D., Gosling, J. T., Lavraud, B., … Goldman, M. V. (2015). On multiple reconnection X-lines and tripolar perturbations of strong guide magnetic fields. *The Astrophysical Journal*, *805*(1), 43.

Fear, R. C., Milan, S. E., Fazakerley, A. N., Lucek, E. A., Cowley, S. W. H., & Dandouras, I. (2008). The azimuthal extent of three flux transfer events. *Annales Geophysicae*, *26*, 2353–2369.

Fedder, J. A., Slinker, S. P., Lyon, J. G., & Russell, C. T. (2002). Flux transfer events in global numerical simulations of the magnetosphere. *Journal of Geophysical Research*, *107*(A5), 1048. https://doi.org/10.1029/2001JA000025

Graham, D. B., Khotyaintsev, Y. V., Norgren, C., Vaivads, A., André, M., Toledo-Redondo, S., … Burch, J. L. (2016). Lower hybrid waves in the ion diffusion and magnetospheric inflow regions. *Journal of Geophysical Research: Space Physics*, *122*, 517–533. https://doi.org/10.1002/2016JA023572

Hasegawa, H., Sonnerup, B. Ö., Owen, C. J., Klecker, B., Paschmann, G., Balogh, A., & Rème, H. (2006). The structure of flux transfer events recovered from cluster data. *Annales geophysicae*, *24*, 603–618.

Hesse, M., Aunai, N., Sibeck, D., & Birn, J. (2014). On the electron diffusion region in planar, asymmetric, systems. *Geophysical Research Letters*, *41*, 8673–8680. https://doi.org/10.1002/2014GL061586

Hesse, M., Schindler, K., Birn, J., & Kuznetsova, M. (1999). The diffusion region in collisionless magnetic reconnection. *Physics of Plasmas*, *6*, 1781.

Hoilijoki, S., Ganse, U., Pfau-Kempf, Y., Cassak, P. A., Walsh, B. M., Hietala, H., … Palmroth, M. (2017). Reconnection rates and X line motion at the magnetopause: Global 2d-3v hybrid-Vlasov simulation results. *Journal of Geophysical Research: Space Physics*, *122*, 2877–2888. https://doi.org/10.1002/2016JA023709

Huba, J. D., Gladd, N. T., & Papadopoulos, K. (1977). The lower-hybrid-drift instability as a source of anomalous resistivity for magnetic field line reconnection. *Geophysical Research Letters*, *4*(3), 125–128.

LaBelle, J., Treumann, R. A., Haerendel, G., Bauer, O. H., Paschmann, G., Baumjohann, W., … Holzworth, R. H. (1987). AMPTE IRM observations of waves associated with flux transfer events in the magnetosphere. *Journal of Geophysical Research*, *92*(A6), 5827–5843.

Lapenta, G., Markidis, S., Divin, A., Goldman, M., & Newman, D. (2010). Scales of guide field reconnection at the hydrogen mass ratio. *Physics of Plasmas*, *17*(8), 082106.

Lapenta, G., Berchem, J., Zhou, M., Walker, R. J., El-Alaoui, M., Goldstein, M. L., … Burch, J. L. (2017). On the origin of the crescent-shaped distributions observed by MMS at the magnetopause. *Journal of Geophysical Research: Space Physics*, *122*, 2024–2039. https://doi.org/10.1002/2016JA023290

Lee, L. C., & Fu, Z. F. (1985). A theory of magnetic flux transfer at the Earth's magnetopause. *Geophysical Research Letters*, *12*(2), 105–108. https://doi.org/10.1029/GL012i002p00105

Malakit, K., Shay, M. A., Cassak, P. A., & Ruffolo, D. (2013). New electric field in asymmetric magnetic reconnection. *Physical Review Letters*, *111*(13), 135001.

Markidis, S., Lapenta, G., & Rizwan-Uddin (2010). Multi-scale simulations of plasma with iPIC3D. *Mathematics and Computers in Simulation*, *80*, 1509–1519.

Mozer, F. S., Wilber, M., & Drake, J. F. (2011). Wave associated anomalous drag during magnetic field reconnection. *Physics of Plasmas*, *18*(10), 102902.

Owen, C. J., Marchaudon, A., Dunlop, M. W., Fazakerley, A. N., Bosqued, J.-M., Dewhurst, J. P., … Reme, H. (2008). Cluster observations of "crater"Ì flux transfer events at the dayside high-latitude magnetopause. *Journal of Geophysical Research*, *113*, A07S04. https://doi.org/10.1029/2007JA012701

Peng, I. B., Markidis, S., Vaivads, A., Vencels, J., Amaya, J., Divin, A., … Lapenta, G. (2015). The formation of a magnetosphere with implicit particle-in-cell simulations. *Procedia Computer Science*, *51*, 1178–1187.

Powell, K. G., Roe, P. L., Linde, T. J., Gombosi, T. I., & De Zeeuw, D. L. (1999). A solution-adaptive upwind scheme for ideal magnetohydrodynamics. *Journal of Computational Physics*, *154*, 284–309.

Price, L., Swisdak, M., Drake, J. F., Cassak, P. A., Dahlin, J. T., & Ergun, R. E. (2016). The effects of turbulence on three-dimensional magnetic reconnection at the magnetopause. *Geophysical Research Letters*, *43*, 6020–6027. https://doi.org/10.1002/2016GL069578

Pritchett, P. L. (2013). The influence of intense electric fields on three-dimensional asymmetric magnetic reconnection. *Physics of Plasmas*, *20*(6), 061204.

Raeder, J. (2006). Flux transfer events: 1. Generation mechanism for strong southward IMF. *Annales Geophysicae*, *24*, 381–392.

Ricci, P., Brackbill, J. U., Daughton, W., & Lapenta, G. (2004). Collisionless magnetic reconnection in the presence of a guide field. *Physics of Plasmas*, *11*, 4102.

Ridley, A., Gombosi, T., & Dezeeuw, D. (2004). Ionospheric control of the magnetosphere: Conductance. *Annales Geophysicae*, *22*, 567–584.

Rijnbeek, R. P., Cowley, S. W. H., Southwood, D. J., & Russell, C. T. (1984). A survey of dayside flux transfer events observed by ISEE 1 and 2 magnetometers. *Journal of Geophysical Research*, *89*, 786–800. https://doi.org/10.1029/JA089iA02p00786

Roytershteyn, V., Daughton, W., Karimabadi, H., & Mozer, F. S. (2012). Influence of the lower-hybrid drift instability on magnetic reconnection in asymmetric configurations. *Physical Review Letters*, *108*(18), 185001.

Russell, C. T., & Elphic, R. C. (1978). Initial ISEE magnetometer results: Magnetopause observations. *Space Science Reviews*, *22*, 681–715.

Shay, M. A., & Drake, J. F. (1998). The role of electron dissipation on the rate of collisionless magnetic reconnection. *Geophysical Research Letters*, *25*, 3759–3762. https://doi.org/10.1029/1998GL900036

Shay, M. A., Drake, J. F., & Swisdak, M. (2007). Two-scale structure of the electron dissipation region during collisionless magnetic reconnection. *Physical Review Letters*, *99*, 155002.

Shay, M. A., Phan, T. D., Haggerty, C. C., Fujimoto, M., Drake, J. F., Malakit, K., … Swisdak, M. (2016). Kinetic signatures of the region surrounding the X line in asymmetric (magnetopause) reconnection. *Geophysical Research Letters*, *43*, 4145–4154. https://doi.org/10.1002/2016GL069034

Sibeck, D. G., Kuznetsova, M., Angelopoulos, V., Glaßmeier, K.-H., & McFadden, J. P. (2008). Crater FTEs: Simulation results and THEMIS observations. *Geophysical Research Letters*, *35*, L17S06. https://doi.org/10.1029/2008GL033568

Tóth, G., Ma, Y. J., & Gombosi, T. I. (2008). Hall magnetohydrodynamics on block adaptive grids. *Journal of Computational Physics*, *227*, 6967–6984.

Tóth, G., Sokolov, I. V., Gombosi, T. I., Chesney, D. R., Clauer, C. R., Zeeuw, D. L. De., … Kóta, J. (2005). Space weather modeling framework: A new tool for the space science community. *Journal of Geophysical Research*, *110*, A12226. https://doi.org/10.1029/2005JA011126

Tóth, G., van der Holst, B., Sokolov, I. V., Zeeuw, D. L. De., Gombosi, T. I., Fang, F., … Opher, M. (2012). Adaptive numerical algorithms in space weather modeling. *Journal of Computational Physics*, *231*, 870–903.

Tóth, G., Jia, X., Markidis, S., Peng, B., Chen, Y., Daldorff, L. K. S., … Dorelli, J. (2016). Extended magnetohydrodynamics with embedded particle-in-cell simulation of Ganymede's magnetosphere. *Journal of Geophysical Research*, *121*, 1273–1293. https://doi.org/10.1002/2015JA021997

Tóth, G., Chen, Y., Gombosi, T. I., Cassak, P., Markidis, S., & Peng, B. (2017). Scaling the ion inertial length and its implications for modeling reconnection in global simulations. *Journal of Geophysical Research*, *122*. https://doi.org/10.1002/2017JA024189

Wang, C.-P., Gkioulidou, M., Lyons, L. R., & Angelopoulos, V. (2012). Spatial distributions of the ion to electron temperature ratio in the magnetosheath and plasma sheet. *Journal of Geophysical Research: Space Physics*, *117*, A08215. https://doi.org/10.1029/2012JA017658

Zhang, H., Kivelson, M. G., Khurana, K. K., McFadden, J., Walker, R. J., Angelopoulos, V., … Auster, H. U. (2010). Evidence that crater flux transfer events are initial stages of typical flux transfer events. *Journal of Geophysical Research*, *115*, A08229. https://doi.org/10.1029/2009JA015013